ADVANCED ENGINEERING MATERIALS
www.aem-journal.com

Deformation Behavior of Optical Ceramic Nanomultilayers: The Role of Aperiodicity

*Danielle E. White, Wenjuan Cheng, Koushik Jagadish, Edoardo Rossi, Yu-Tsun Shao, and Andrea M. Hodge**

Aperiodicity in ceramic nanomultilayers (NMs) has been shown to improve coating functionality, namely, for optimized optical behavior, while the effects of aperiodic layer thicknesses on mechanical deformation remain poorly understood. In this article, the relationships between individual layer thicknesses, optical transmittance, and mechanical behavior are investigated for AlN/Al_2O_3, YSZ/Al_2O_3, and AlN/YSZ nanomultilayered coatings. These NMs are synthesized with aperiodic layer configurations from individual constituents selected for their optical constants, elastic modulus, and hardness values; the layer designs of select samples are optimized to achieve a transmittance exceeding 90% across the ultraviolet, visible, and near-infrared spectral range. The effect of aperiodicity on the mechanical properties and deformation is explored at various length scales via nanoindentation, micropillar splitting, and Vickers microindentation. However, competing factors, such as interface type and local microstructure, also play critical roles. It is observed that layer composition strongly influences fracture toughness, as samples with amorphous Al_2O_3 layers and crystalline/amorphous interfaces exhibit superior mechanical performance and the highest fracture toughness values. Yet, distinct failure modes, including delamination and intergranular fracture, across the different nanomultilayered architectures highlight the relation of optical and mechanical properties to local volume fractions within aperiodic layer stacks and interface characteristics in the coating design.

1. Introduction

Nanomultilayers (NMs) are coatings consisting of stacked nanometer-thick layers, leading to a density of interfaces that enables a higher degree of material property tunability when compared to single-layered coatings. More specifically, ceramic NMs can be designed with constituents such as AlN, Al_2O_3, SiO_2, Ta_2O_5, TiO_2, and ZrO_2 to exploit their broadband transmittance, namely, in the ultraviolet, visible, and near-infrared (UV-Vis-NIR) spectral wavelength range, in addition to their chemical inertness, thermal stability, and high hardness.[1,2] Consequently, NMs are useful as infrared windows and mirrors, antireflection, anticorrosion, and wear-resistant coatings for cutting machinery.[3–5] Applications that require mechanical functionality of ceramic NMs can be linked to tribological studies, which have shown improvement in mechanical properties by altering the number of bilayers, interfacial density, and/or layer morphology.[6–10] For example, epitaxial growth occurred at critical bilayer thicknesses in various ceramic NMs, resulting in superlattice NM microstructures with superior hardness.[11–13] Similarly, layer thickness can be tuned for optical functionality in ceramic NMs, where optimized optical performance via aperiodicity has been demonstrated.[1,14–16] However, linking optical tunability to mechanical failure is poorly understood yet intricately linked.

In general, deterioration of optical properties in coatings often is correlated to an environmental event, such as heat exposure, irradiation, or abrasion/particle impact. These external factors can cause the onset of degradation mechanisms, including oxidation and/or stress-induced crack growth, which can lead to optical scatter or loss.[3,17] For example, Putz et al. studied the optical performance and thermomechanical stability of Inconel/Ag bilayers via thermal cycling, observing that the induced crack and void formation lowered coating reflectivity.[18] The effects of degradation mechanisms in optical coatings typically are linked to the behavior of unique compositions, and yet, are seldomly compared to additional coating features.[18,19] Considering that aperiodicity is utilized as an optimization tool in optical NMs, there is an opportunity to understand the response of aperiodic layers to coating degradation mechanisms. Specifically for optical ceramic NMs,

D. E. White, K. Jagadish, Y.-T. Shao, A. M. Hodge
Mork Family Department of Chemical Engineering and Materials Science
University of Southern California
925 Bloom Walk, Los Angeles, CA 90089, USA
E-mail: ahodge@usc.edu

W. Cheng, E. Rossi
Civil, Computer Science and Aeronautical Technology Engineering
Università degli Studi Roma Tre
Via della Vasca Navale, 79, 00146 Rome, Italy

The ORCID identification number(s) for the author(s) of this article can be found under https://doi.org/10.1002/adem.202501269.

DOI: 10.1002/adem.202501269

deformation studies of optical ceramic NMs are limited in both scope and number, as attention has been focused primarily on linking mechanical properties to coating features, such as the number of layers, bilayer thickness, and/or morphology.[14,15,20,21] In addition to the testing challenges for thin films (a fraction of a nanometer to a few microns in thickness), factors such as sample preparation, grain orientation, load and strain rate sensitivity, and defect density for brittle materials may lead to premature failure, further affecting how the mechanical behavior of ceramic NMs is interpreted.[22,23] To avoid these testing issues, plastic deformation prior to failure is commonly studied via semi-destructive indentation techniques, such as nanoindentation and Vickers microindentation.[24–26] Specifically, nanoindentation is a typical tool to investigate the mechanical behavior of NMs, from which the coating elastic modulus E and hardness H are derived and can be related to the repeated bilayer thickness, superlattice architectures, and/or residual stress, for example.[25,27,28] Vickers microindentation, when combined with cross-sectional microscopy, can be used for qualitative insights on fracture behavior to clarify the roles of residual stress, layer-to-layer interactions, and interfaces under deformation.[29–31] Nonetheless, the brittle characteristics of ceramic NMs clearly emphasize the need to study their fracture toughness, which is also directly coupled to the final optical functionality of NMs. In thin film mechanics, techniques such as microcantilever bending and micropillar splitting have been implemented and developed to evaluate fracture toughness.[32,33] In microcantilever bending, the fracture toughness is typically derived from the critical load at which the beam fractures, allowing for the evaluation of crack initiation and propagation within individual layers or interfaces.[34] In micropillar splitting, a sharp indenter is used to apply axial load on microfabricated cylindrical pillars until catastrophic fracture occurs. The apparent fracture toughness (i.e., the overall crack propagation resistance of the coating) is estimated from the critical splitting load P_c, the pillar radius R, and a dimensionless coefficient γ, as detailed in the literature.[35] When micropillar splitting is coupled with fractography, deformation can be linked to interfaces, layer thickness, and even elastic modulus and hardness through fracture toughness calculations.[23,24,33,35–40] Overall, the aforementioned techniques can be incorporated into NM studies to provide a comprehensive investigation of the global mechanical behavior for optical-mechanical optimization.

Given the complexities in understanding the mechanical failure in optical NMs, studies of nonoptical repeated bilayer configurations can provide valuable insights on deformation and fracture, serving as foundational guides for connecting mechanical behavior with individual layer thicknesses and crystallinity. For example, a previous work on crystalline/crystalline (C/C) Al_2O_3/TiO_2 NM tested via spherical indentation exhibited extensive deformation, which was attributed to columnar grain reorientation, sliding, and relocation.[29] A micropillar compression study of crystalline/amorphous (C/A) Cu/Al_2O_3 NMs demonstrated that 10 nm amorphous Al_2O_3 layers inhibited shear localization.[41] Likewise, a study of C/A Al/Al_2O_3 NMs under tension observed a transition in fracture mechanisms as the Al_2O_3 thickness was increased from 2.4 to 9.4 nm.[42] However, the applicability of repeated bilayer deformation and failure to that of aperiodic NMs remains unknown, highlighting a crucial gap in understanding the roles of individual layers and stack configurations, especially when linked to optical materials.

In this work, AlN/Al_2O_3 (C/A), YSZ/Al_2O_3 (C/A) (YSZ is 8 mol% yttria-stabilized zirconia), and AlN/YSZ (C/C) NM systems were synthesized with aperiodic layers and similar constituent volume fractions, where one sample from each system was optimized for a minimum average transmittance of 90% across the UV-Vis-NIR wavelength spectrum. Spectrophotometry and nanoindentation measurements were performed for all NM samples and on single-layer AlN, Al_2O_3, and YSZ coatings, which provide baseline values. Additionally, for the NMs, fracture toughness and layer deformation were evaluated via a combination of micropillar splitting, Vickers indentation and postmortem scanning electron microscopy (SEM) and transmission electron microscopy (TEM) cross-section images. Overall, trends in deformation and fracture were established and linked to aperiodicity and layer constituents, which can facilitate the design of robust ceramic coatings. Within the scope of optical ceramic NMs, insights on the roles of ceramic layers and local volume fractions connect aperiodicity with optical transmittance and fracture toughness, suggesting a path toward joint optomechanical tunability.

2. Results and Discussion

To investigate the influence of aperiodic layers on optomechanical functionality in ceramic NMs, a total of five aperiodic NMs were synthesized from the AlN/Al_2O_3, YSZ/Al_2O_3, and AlN/YSZ systems. For all NMs, regardless of periodicity, the volume fraction for the second layer constituent was constrained to ≈70%–80% for comparison purposes. More specifically, one layer configuration for each system was modeled via the multiple-beam-interference (MBI) recursive method to ensure a minimum predicted UV-Vis-NIR transmittance of 90%.[20,43,44] Here, the optically optimized NMs are referred to as YSZ/Al_2O_3 MBI 74, AlN/YSZ MBI 82, and AlN/Al_2O_3 MBI 78, where "MBI" refers to an optically optimized configuration, and the numerical portion of the sample name refers to the modeled volume fraction of the second layer constituent. For example, YSZ/Al_2O_3 MBI 74 is predicted to have an overall Al_2O_3 volume fraction of 0.74. Furthermore, nonoptically optimized NM samples of the AlN/YSZ and YSZ/Al_2O_3 systems were synthesized with similar layer distributions to AlN/Al_2O_3 MBI 78 to compare transmittance and deformation based on layer thicknesses.

Figure 1 presents an overview of the layer configuration and characteristics for the modeled and as-sputtered NMs. Figure 1a provides a visual representation of the aperiodic distribution of layers for the NMs. Following the sputtering direction, which begins at the bottom of each schematic and moves upwards through the layers, local variations of volume fraction can be observed based on groupings of layers, herein referred to as layer stacks. For instance, in AlN/Al_2O_3 MBI 78, the stack of layers 1–16 are modeled with a locally high Al_2O_3 volume fraction stack of 0.94; this is topped by a stack (layers 17–20) in which the AlN volume fraction is 0.73. The layer stacking for YSZ/Al_2O_3 78 and AlN/YSZ 78 is similarly distributed. In contrast, YSZ/Al_2O_3 MBI 74 and AlN/YSZ MBI 82 are modeled with five and three distinct layer stacks, respectively.

Figure 1b shows the X-ray diffraction data for single-layered coatings of AlN, Al_2O_3, and 8 mol% YSZ. For the AlN film, a

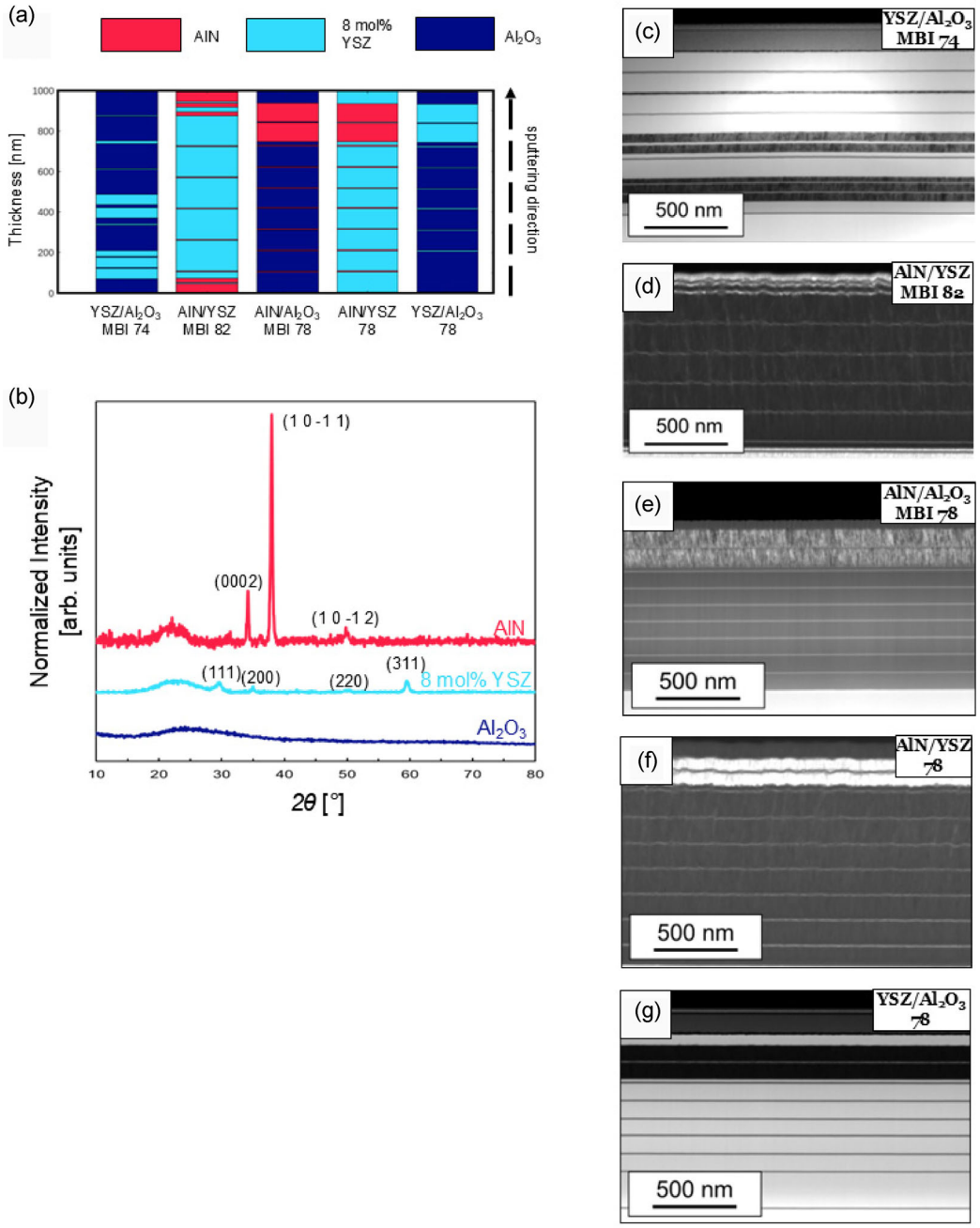

Figure 1. Layer design and characterization overview. a) Schematic of aperiodic ceramic NMs. b) Diffraction plots of AlN, 8 mol% YSZ, and Al_2O_3 single-layered coatings. As-sputtered cross-section of c) YSZ/Al_2O_3 MBI 74, d) AlN/YSZ MBI 82, e) AlN/Al_2O_3 MBI 78, f) AlN/YSZ 78, and g) YSZ/Al_2O_3 78 NMs. The numerical portion of the multilayer sample name indicates the modeled % volume fraction of the second layer constituent, whereas "MBI" refers to a layer configuration that was designed to yield a minimum UV-Vis-NIR transmittance of 90%.

hexagonal (1 0−1 1) texture is visible, whereas the YSZ coating exhibits the cubic phase, with no preferential orientation of the (1 1 1), (2 0 0), (2 2 0), or (3 1 1) planes, and Al_2O_3 is X-ray amorphous. Additionally, all patterns exhibit a diffuse peak in the 20°–30° 2θ range due to scattering from the glass substrate. The observed X-ray patterns are supported by microstructural characterization in prior studies and representative of the individual layers within the NMs of the current study.[21,45,46] Henceforth, AlN/Al_2O_3 and YSZ/Al_2O_3 NMs will be noted as having C/A layers, and AlN/YSZ, C/C layers. Figure 1c–g shows representative cross-sectional scanning TEM (STEM) images for the YSZ/Al_2O_3, AlN/YSZ, and AlN/Al_2O_3 NMs that were deposited under the same conditions as the single-layered coatings. While the as-sputtered NM layer thicknesses deviate slightly from the coating designs (Figure 1a), the aperiodic layer distribution within each coating is preserved. Additionally, the

cross-sectional images demonstrate sharp layer termination, although the C/C AlN/YSZ NMs exhibit more layer roughness than the C/A systems. Similar observations of interface roughness have been reported in various C/C NM systems and attributed to deposition conditions.[6,47] It also was observed that a higher degree of interface/surface roughness can lower optical functionality, and therefore, the transmittance of the C/C NMs may be affected, which is most important for optically optimized samples.[48,49] However, since the indices of refraction for the individual layers of AlN, Al_2O_3, and YSZ are 2.18, 1.77, and 1.63, respectively, optical optimization can be achieved by alternating layers of high- and low-indices of refraction or by having low refractive indices for both layers.[1,14–16,50–52] To further explore the layer stacking, distributions, and characteristics, the role of aperiodicity on optical transparency (Section 2.1) and mechanical deformation (Section 2.2) is assessed.

2.1. Optical Transmittance

The effect of aperiodic layers on optical behavior for the ceramic NMs was measured in the UV-Vis-NIR spectra, where **Figure 2** shows the transmittance versus wavelength curves for the YSZ/Al_2O_3, AlN/YSZ, and AlN/Al_2O_3 NMs from 380 to 1100 nm, plotted alongside representative sample images for visual comparison of transparency. Additional optical results for all single-layered and NM coatings are compared in **Table 1**, which includes the layer crystallinity, modeled optical transmittance as calculated by implementation of the MBI method, and as-sputtered optical transmittance that was measured experimentally (see Experimental Section). The average experimental transmittance for the optically optimized NMs is 91.0%, which is higher than that of the nonoptically optimized NMs (88.7%). Closer examination of the optically optimized NMs reveals that YSZ/Al_2O_3 MBI 74 demonstrates a transmittance between that of the YSZ and Al_2O_3 single-layered coatings. Similarly, AlN/YSZ MBI 82 and AlN/Al_2O_3 MBI 78 exhibit values between those of their respective layer constituents. Among all NMs, however, YSZ/Al_2O_3 78 achieved the highest average experimental transmittance of 95.2%. Discrepancies between experimental and predicted optical values are expected since optical inputs for the UV-Vis-NIR spectra are considered constant when implementing the MBI method in this study. Particularly, the refractive indices used for AlN, Al_2O_3, and 8 mol% YSZ were determined by single-point ellipsometry at 550 nm, whereas spectroscopic refractive indices tend to fluctuate across a wide wavelength spectrum.[53–56] Furthermore, while the thickness of each layer is accounted for in the transmittance predictions, as-sputtered deviations and layer morphology are not considered, although directly correlated to optical behavior. For example, the refractive index was linked to layer porosity of SiO_2 coatings, which was altered by adjusting the angle of deposition.[52] In a separate study, the optical transmittance and reflectance of multilayers were significantly affected by an interface roughness on the order of 3 nm.[49] While all optically optimized NMs in this study met the minimum performance requirement of a 90% UV-Vis-NIR transmittance, additional coating designs, prediction inputs, and deposition parameters can be adjusted to further improve the estimates and increase experimental transmittance. The wide range of material selection is especially beneficial for optomechanical NMs, in which layer constituents should contribute to coating toughness as well.

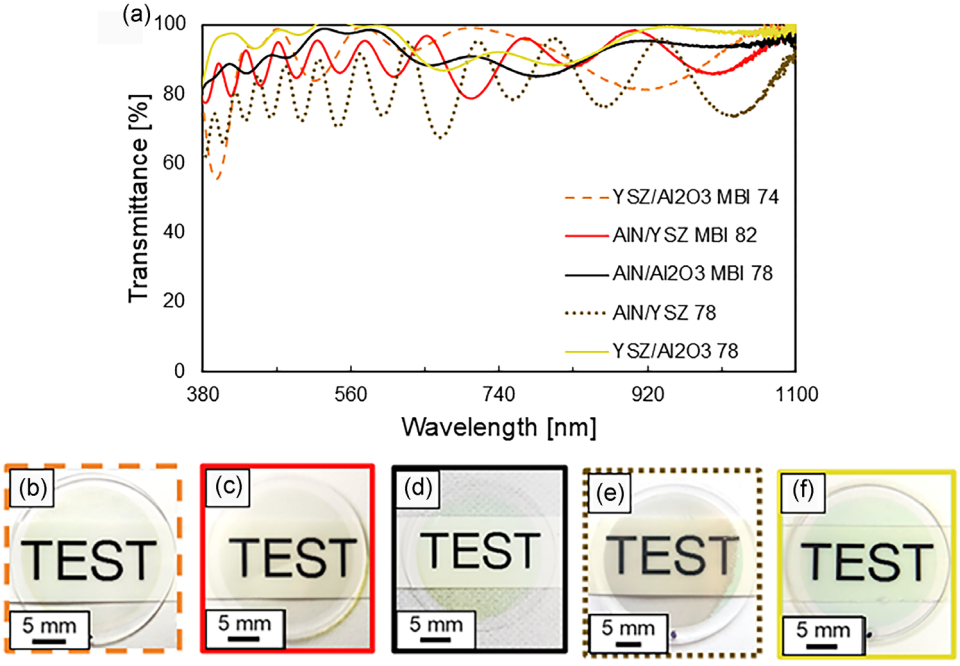

Figure 2. UV-Vis-NIR transmittance for aperiodic NMs. a) Experimental optical transmittance of aperiodic ceramic NMs plotted from 380 to 1100 nm. b–f) show representative top-view images of as-sputtered nanomultilayered coatings deposited onto Corning Eagle 2000 substrates, color-coded to correspond with the respective transmittance plot. The numerical portion of the sample name indicates the modeled % volume fraction of the second layer constituent, whereas "MBI" refers to a layer configuration that was designed to yield a minimum UV-Vis-NIR transmittance of 90%.

Table 1. As-Sputtered crystallinity, modeled, and experimental UV-Vis-NIR transmittance of ceramic single layers and aperiodic NMs. The numerical portion of the NM name indicates the modeled % volume fraction of the second layer constituent, whereas "MBI" refers to a layer configuration that was designed to yield a minimum UV-Vis-NIR transmittance of 90%.

Sample	Layer crystallinity	Modeled optical transmittance, 380–1100 nm [%]	Experimental optical transmittance, 380–1100 nm [%]
AlN	C	82.9	92.1
Al_2O_3	A	92.0	96.6
YSZ	C	84.8	88.9
YSZ/Al_2O_3 MBI 74	C/A	95.4	90.7
AlN/YSZ MBI 82	C/C	95.3	90.2
AlN/Al_2O_3 MBI 78	C/A	93.2	92.1
AlN/YSZ 78	C/C	79.0	82.1
YSZ/Al_2O_3 78	C/A	93.8	95.2

2.2. Mechanical Behavior: Deformation and Properties

As previously stated, the mechanical testing of ceramic NM coatings can be intricate due to the brittle nature of ceramics and thin films coupled with limited number and scope of mechanical studies. Yet, by implementing several techniques across various length scales and testing modes, a comprehensive view of deformation in aperiodic ceramic NMs can be obtained. For this purpose, the YSZ/Al_2O_3, AlN/YSZ, and AlN/Al_2O_3 NMs were tested via nanoindentation, micropillar splitting, and Vickers microindentation, providing both quantitative and qualitative comparisons. **Table 2** contains testing results from profilometry, nanoindentation, and pillar splitting, with the columns showing the residual stress, elastic modulus, hardness, and fracture toughness for both single-layered and NM coatings. Here, the single-layered samples are used as baselines for comparison to the rule of mixtures (RoM).[57] All samples have a residual stress magnitude lower than 1 GPa. Although the exact values range from −787.6 to 89.6 MPa, most samples are compressive, barring Al_2O_3 and AlN/YSZ MBI 82. In general, many factors affect the coatings' residual stress states, as it has been reported that sputtered thin films tend to develop compressive stresses, while columnar grains with intergranular voids can induce tensile stresses, and thermal expansion mismatch influences the overall residual stress profile.[58–61] For example, variations in the residual stress values of the AlN/YSZ NMs highlight the complexity of competing factors, such as layer thickness which, in turn, can influence mechanical properties.[8,55,58,62] Consequently, nanoindentation was performed to assess the elastic modulus and hardness of the single-layered and NM coatings. For the NMs, the elastic modulus ranges from 142.5 to 174.8 GPa, with all values being statistically significant (two-sided, two-sample *t*-test, *P*-value of 0.001).[63] AlN/YSZ 78 and AlN/YSZ MBI 82 present the highest and lowest modulus, respectively. When compared to the single-layered coatings, the elastic moduli for YSZ/Al_2O_3 MBI 74, AlN/YSZ MBI 82, AlN/YSZ 78, and YSZ/Al_2O_3 78 are within the calculated bounds from the RoM.[57] Similarly, the hardness of the NMs varies from 10.9 to 16.0 GPa, with all values being statistically significant, except for AlN/YSZ 78 and YSZ/Al_2O_3 78.[63] It should be noted that YSZ/Al_2O_3 MBI 74 and YSZ/Al_2O_3 78 contain similar constituent volume fractions but different hardness values (12.9 GPa vs. 15.6 GPa), and a similar trend was observed for AlN/YSZ MBI 82 and AlN/YSZ 78 (10.9 GPa vs. 16.0 GPa). Therefore, further tunability of mechanical behavior in the aperiodic ceramic NMs can be enabled by examining the contributions of individual layers through additional testing techniques, expanding the correlation between coating features and deformation mechanisms.

Table 2. Residual stress, elastic modulus, hardness, and fracture toughness of ceramic single layers (from literature) and aperiodic NMs (experimental). The numerical portion of the NM name indicates the modeled % volume fraction of the second layer constituent, whereas, "MBI" refers to a layer configuration that was designed to yield a minimum UV-Vis-NIR transmittance of 90%.

Sample	Residual stress [MPa]	*E* [GPa]	*H* [GPa]	K_c [MPa*$\sqrt{m}$]
AlN	−17.2	148.8 ± 4.6	9.1 ± 0.7	1.5–1.8[72]
Al_2O_3	89.6	109.4 ± 3.7	6.4 ± 0.5	2.5–3.8[72,73]
YSZ	−2.5	172.4 ± 19.0	11.1 ± 2.4	≈1.2–1.7[74,75]
YSZ/Al_2O_3 MBI 74	−787.6	152.2 ± 3.4	12.9 ± 1.3	3.4 ± 0.5
AlN/YSZ MBI 82	2.2	142.5 ± 8.1	10.9 ± 0.7	1.6 ± 0.3
AlN/Al_2O_3 MBI 78	−38.3	161.2 ± 3.7	13.8 ± 0.5	2.9 ± 0.2
AlN/YSZ 78	−139.6	174.8 ± 6.9	16.0 ± 1.8	1.7 ± 0.2
YSZ/Al_2O_3 78	−612.7	166.9 ± 3.6	15.6 ± 0.8	3.5 ± 0.2

The evaluation of fracture toughness was performed on the YSZ/Al_2O_3, AlN/YSZ, and AlN/Al_2O_3 NMs via micropillar splitting, using the nanoindentation-derived elastic modulus and hardness for calculations based on Equation (1) in the Experimental Section.[35] It should be noted that the single-layered fracture toughness (K_C) values were derived from various and/or unspecified loading modes, whereas the nanomultilayered fracture toughness values are correlated to mode I loading (opening, K_{IC}). The fracture toughness values are shown in the last column of Table 2 and further discussed in **Figure 3**, where the load-displacement curves for each NM are shown with representative SEM image insets of postmortem pillars. It is observed that YSZ/Al_2O_3 78 exhibits the highest apparent fracture toughness of 3.5 MPa$\sqrt{m}$, followed by 3.4 MPa$\sqrt{m}$ for YSZ/Al_2O_3 MBI 74 and 2.9 MPa$\sqrt{m}$

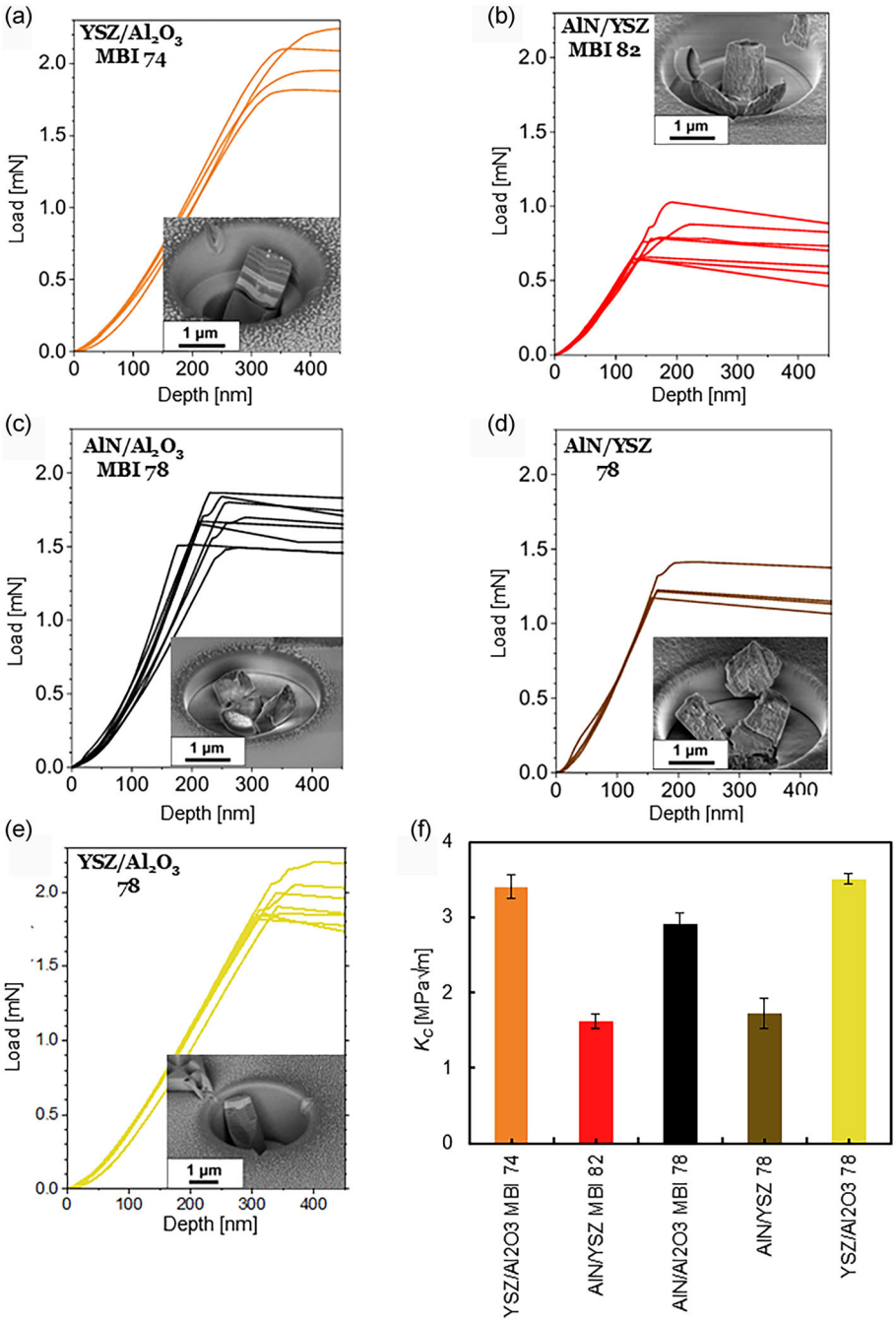

Figure 3. Pillar splitting. Representative load-displacement curves obtained for aperiodic a) YSZ/Al_2O_3 MBI 74, b) AlN/YSZ MBI 82, c) AlN/Al_2O_3 MBI 78, d) AlN/YSZ 78, and e) YSZ/Al_2O_3 78 NMs during pillar splitting tests with corresponding postfracture SEM micrographs as insets. f) Bar graph of average apparent fracture toughness for all NMs.

for AlN/Al_2O_3 MBI 78. AlN/YSZ 78 and AlN/YSZ MBI 82 exhibit relatively lower fracture toughness values of 1.7 and 1.6 $MPa\sqrt{m}$, respectively (Table 2). These values also are depicted in a bar graph in Figure 3f. Since the fracture toughness for ceramic materials typically spans from 1 to 3 $MPa\sqrt{m}$, the attained values for all NMs are expected, and separately, are intermediate to those of their constituents, with the YSZ/Al_2O_3 NMs presenting the highest values.[57] Specifically for the NMs, apparent fracture toughness was derived from an equation based on the critical splitting load, pillar radius, and γ, a coefficient influenced by the E/H ratio, Poisson's ratio, and the indenter angle (see Equation (1) in Experimental Section).[35] It was previously reported for ceramic NMs that, when comparing the weight of various factors, the critical splitting load is a direct parameter to evaluate fracture toughness. Hence, the fracture behavior of the aperiodic ceramic NMs is further analyzed through their load-displacement curves, where

the critical pillar splitting load is defined as the load at which unstable crack growth occurs, characterized by a displacement burst and discontinuity at relatively shallow depths.[32] In all, YSZ/Al_2O_3 MBI 74 and YSZ/Al_2O_3 78 exhibit the highest critical splitting loads, averaging 2.0 and 1.9 mN, respectively. These are followed by AlN/Al_2O_3 MBI 78 (1.7 mN), AlN/YSZ 78 (1.2 mN), and AlN/YSZ MBI 82 (0.8 mN). A displacement burst for AlN/YSZ MBI 82 (Figure 3b), AlN/Al_2O_3 MBI 78 (Figure 3c), and AlN/YSZ 78 (Figure 3d) occurs ≈200 nm into the coating and at a depth of ≈300 nm for YSZ/Al_2O_3 78 (Figure 3e). Interestingly, although similar critical loads were observed in the YSZ/Al_2O_3 NMs, an inflection point rather than a displacement burst is noted for YSZ/Al_2O_3 MBI 74 (Figure 3a), which is an uncharacteristic behavior for pillar splitting and can be indicative of stable crack growth.[32]

The postfracture SEM image insets of Figure 3 indicate that the C/C AlN/YSZ NMs failed by intergranular fracture (Figure 3b,d), where the step-like features on the fracture surfaces for AlN/YSZ 78 suggest crack deflection at the interfaces, a behavior known as a toughening mechanism for NMs.[38] For C/A AlN/Al_2O_3 MBI 78, the intergranular fracture mode is confined to the layer stack with a locally high AlN volume fraction (Figure 3c). However, the fracture surfaces for the C/A YSZ/Al_2O_3 NMs are relatively featureless (Figure 3a,e). Overall, when comparing measured values and postmortem images of the C/C and C/A NMs, the latter seems more suitable for mechanical functionality, although the opportunity for improvement remains. Specifically, previous studies on C/A NMs and nanolaminates reported that failure modes can be controlled through the amorphous layer thickness.[30,64,65] Thus, the C/A NMs in this work were selected for additional testing, through which the link of aperiodicity to deformation could be further developed.

To explore the qualitative effects of aperiodic configurations, Vickers microindentation was performed at a 0.245 N (25-gf) load, as shown in **Figure 4** for the three C/A NMs, which includes representative top-surface SEM indent images (Figure 4a), cross-sectional high-angle annular dark-field (HADDF-STEM) micrographs (Figure 4b), and magnified views of the cross-sections (Figure 4c). (To view top-surface SEM images of Vickers indents for all NMs, see Figure S1, Supporting Information). From the SEM images in Figure 4a, fracture features are observed for AlN/Al_2O_3 MBI 78 (Figure 4a1) and YSZ/Al_2O_3 78 (Figure 4a2), with cracks formed around the indent edge. In contrast, no distinct fracture features are noted for YSZ/Al_2O_3 MBI 74, which is the only NM with a locally high amorphous volume fraction stack near the surface of the coating (see Figure 1). This is consistent with the unique yielding of YSZ/Al_2O_3 MBI 74 observed during the pillar splitting tests. To connect top-surface indentation observations with layer-specific deformation and local volume fractions, electron-transparent cross-sections were prepared under the horizontal indent diagonals for the C/A NMs (as outlined in Figure 4a1), with STEM micrographs of the cross-sections provided in Figure 4b,c. From these images, it is observed that the substrates and coatings bend in response to the applied load, confirming flexure of the coating. For AlN/Al_2O_3 MBI 78, delamination, reoriented grains, and intergranular fracture are observed within a locally high AlN volume fraction stack (Figure 4b1). Whereas, YSZ/Al_2O_3 78 and YSZ/Al_2O_3 MBI 74 do not exhibit any fracture features within its layers (Figure 4b2,b3). These observations are consistent with a previous study on TiAlN coatings

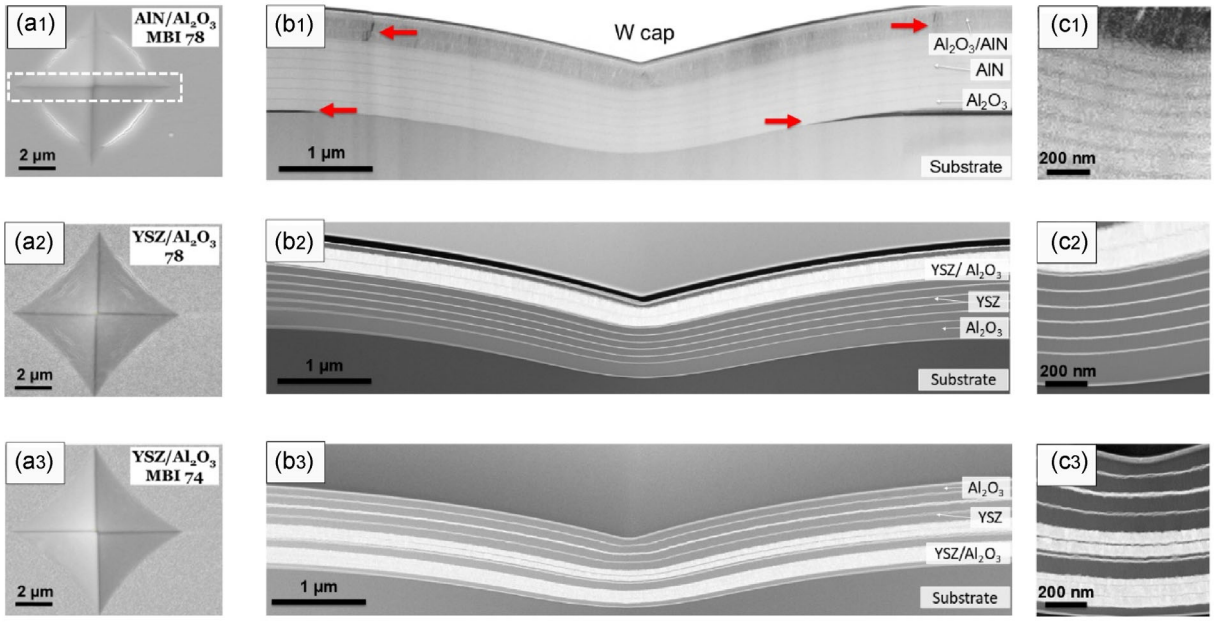

Figure 4. Vickers indentation and cross-sectional analysis. Representative micrographs post Vickers indentation at 25 gf for aperiodic ceramic NMs. Planview SEM of a1) AlN/Al_2O_3 MBI 78, a2) YSZ/Al_2O_3 78, and a3) YSZ/Al_2O_3 MBI 74 indents. b1–b3) Corresponding cross-sectional HAADF-STEM micrographs along the indent diagonal, as marked by the dashed box in (a1). Red arrows in (b1) indicate areas of deformation or delamination. c1–c3) Magnified views of corresponding samples. The numerical portion of the NM name indicates the modeled % volume fraction of the second layer constituent, whereas "MBI" refers to a layer configuration that was designed to yield a minimum UV-Vis-NIR transmittance of 90%. (a1–c1) modified from Thin Solid, Films, 815, Synthesis and characterization of aperiodic multifunctional AlN/ Al_2O_3 NMs.[30] Copyright (2025), with permission from Elsevier.

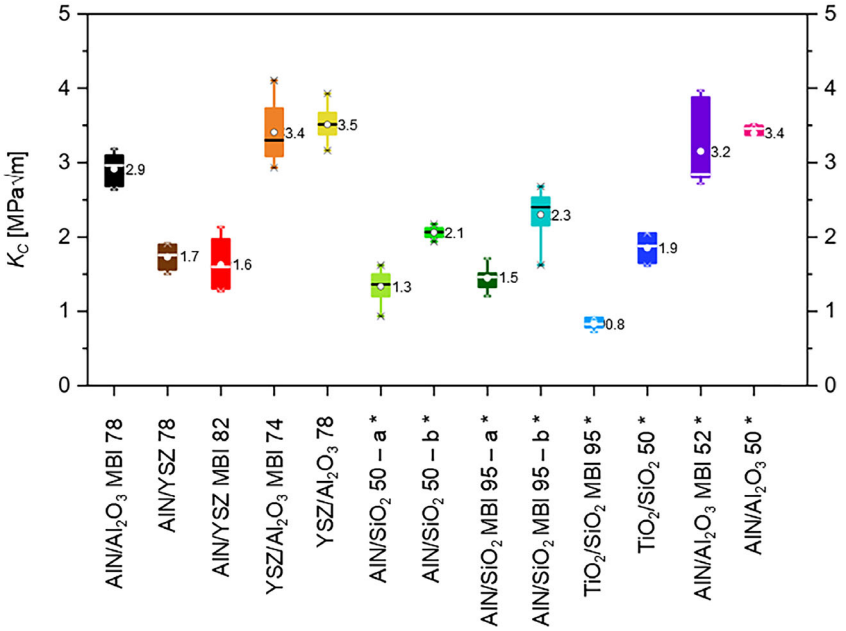

Figure 5. Fracture toughness. Fracture toughness as determined by pillar splitting for ceramic NMs. The numerical portion indicates the modeled % volume fraction of the second layer constituent, where all samples with "50" are comprised of a repeated bilayer configuration with 50 nm-thick layers. "MBI" refers to a layer configuration that was designed to yield a minimum UV-Vis-NIR transmittance of 90%. The (*) symbol designates samples from prior work.[14]

which suggested that larger compressive stresses (see Table 2) allow for greater compensation of strain.[66] Furthermore, independent of magnitude and compressive stresses are known to retard crack propagation and counter the effects from tensile loads.[5]

To further visualize the design space for ceramic optical NMs, the experimental fracture toughness values for NM systems with repeated bilayer and aperiodic layer configurations from current and previous work are presented in **Figure 5**.[14] The plotted NMs include AlN, Al_2O_3, 8 mol% YSZ, SiO_2, and TiO_2 as layer constituents in C/C, C/A, and amorphous/amorphous (A/A) NM systems. The highest fracture toughness values are attributed to Al_2O_3-containing NMs in C/A systems, ranging from 2.9 to 3.5 MPa$\sqrt{m}$. The C/A AlN/SiO_2 NMs present lower values of 1.3 to 2.3 MPa$\sqrt{m}$. In contrast, A/A TiO_2/SiO_2 and C/C AlN/YSZ NMs have fracture toughness values ranging from 0.8 to 1.9 MPa$\sqrt{m}$. Additionally, the variations in fracture toughness within each NM system indicate that layer structures affect fracture behavior. More specifically, varying the local volume fraction via aperiodic layer stacking has been shown to induce different types of failure modes, indicating that the fracture path can be tailored. By linking the NM fracture toughness and deformation to various factors, including materials selection, interface type, and layer stacking, the design of new aperiodic ceramic NMs can be tuned with distinct fracture features for optical and nonoptical applications.

3. Conclusion

In this work, aperiodic ceramic NMs were studied to explore the role of various layer arrangements on optical transmittance and mechanical behavior. NMs with similar and distinct layer stacks across the AlN/Al_2O_3, YSZ/Al_2O_3, and AlN/YSZ systems were synthesized to enable this investigation, with one configuration for each system designed for optical optimization. A minimum 90% transmittance across the UV-Vis-NIR wavelength spectrum was achieved for the optically optimized aperiodic NMs, highlighting opportunities to further increase transmittance and examine the mechanical behavior through the scope of aperiodicity. By performing mechanical tests at various length scales, the influences of aperiodic layer stacking, C/C and C/A interfaces, and localized volume fractions were evident when comparing properties, such as hardness and fracture toughness, within and across the systems. Samples with amorphous Al_2O_3 layers and C/A interfaces generally demonstrated the best mechanical performance, and specifically for the YSZ/Al_2O_3 MBI 74 NM coating, indications of stable crack propagation and strain accommodation without fracture were noted. Thus, the scope and span of the mechanical behavior presented in this study elucidate the correlation between aperiodicity and deformation in optical ceramic NMs, where variations in local volume fraction within aperiodic configurations can be tailored to control the fracture mode. This demonstrates that, although interface characteristics and layer composition influence deformation, aperiodicity can be implemented as a design factor for optomechanical multifunctionality.

4. Experimental Section

Coating Synthesis: AlN/Al_2O_3, AlN/YSZ, and YSZ/Al_2O_3 NMs and single-layered AlN, Al_2O_3, and YSZ coatings were synthesized via magnetron sputtering on Corning Eagle 2000 boro-aluminosilicate substrates

(Delta Technologies, Colorado), 25 mm in diameter and 0.5 mm in thickness. All single layer and NM coatings were deposited with targeted overall thicknesses of ≈1 μm. Substrates were cleaned with a 1:1 isopropanol and acetone mixture. Before deposition, the sputtering chamber was evacuated to a base pressure less than 1.0×10^{-4} Pa. AlN layers were deposited via reactive DC sputtering with a 33 mm (1.3-inch), 99.99% Al target (Plasmaterials, California). Power was set to 150 W, and the argon (Ar) and nitrogen (N_2) gas flow rates were 37.5 and 12.5 sccm, respectively, resulting in a working pressure of 1.2 Pa. Al_2O_3 layers were deposited via radio frequency sputtering with 33 mm (1.3-inch), 99.99% Al_2O_3 target. Power settings were fixed at 40 W with a tune of 38% and load of 76%. Inert Ar pressure was set at 0.67 Pa. The synthesis parameters for AlN and Al_2O_3 follow sputtering conditions in previous works.[14,21] YSZ layers were deposited with a 99.7% $(ZrO_2)92(Y_2O_3)08$ mol% target, using the same power and gas settings as Al_2O_3. All oxide layers were deposited with the same stoichiometry as the target. All targets were manufactured by Plasmaterials (California). Regarding the sputtering configuration for NM coatings, the chamber was equipped with two sources, and power was alternately routed to one of two targets, with 5 min allotted between the deposition of each layer for vapor evacuation.

Optical Design and as-Sputtered Characterization: Optically optimized, aperiodic layer structures and the predicted UV-Vis-NIR transmittance (380–1100 nm) for AlN/Al_2O_3, YSZ/Al_2O_3, and AlN/YSZ NM systems were modeled by implementing the MBI recursive method in an in-house MATLAB code.[20,43,44] Experimental transmittance was measured for all samples from 200 to 1100 nm with a Cary UV-Vis 60 Spectrophotometer (Agilent, California). Residual stress was calculated using Stoney's equation, where the Alpha-Step D-600 stylus profilometer (KLA Corporation, California) was used to obtain 24-mm-long profiles of the radius of curvature, R, centered across the substrates before and after deposition.[25]

To prepare as-sputtered NM cross-sections, a Helios 5CX Dual Beam Microscope (Thermo Fischer Scientific, Massachusetts) was used. The procedure for lamellae extraction and STEM imaging followed a standard lift-out and thinning approach to achieve a final lamella thickness of less than 80 nm. Initially, the region of interest was coated with a protective layer to preserve near-surface features. A 200-nm-thick platinum (Pt) layer was deposited using electron beam deposition at 5 kV and 1.4 nA. Subsequently, a 2-μm-thick tungsten (W) layer was deposited using ion beam deposition at 30 kV and 0.79 nA. Trenches were milled using the ion beam at 30 kV and 0.79 nA to define the lamella dimensions of $\approx 15 \times 5$ μm (depth) with an initial thickness of 1.5 μm for extraction. The lamella was then lifted out and attached to a copper grid for subsequent thinning in three sequential steps to achieve electron transparency: 1) coarse thinning was conducted at 30 kV and 0.23 nA, 2) fine polishing was carried out at 30 kV and 80 pA, and 3) low-energy polishing at 5 kV and 15 pA was applied to minimize surface damage and achieve a final thickness of less than 80 nm. The analysis of the lamellae was performed in STEM mode (STEM 3+ detector) using an acceleration voltage of 30 kV and a current of 0.34 nA, in both brightfield and darkfield, with a dwell time of 30 μs and a line integration of 2.

Nanoindentation: For the single-layered coatings, load-controlled nanoindentation was performed in a 10×10 array with a Hysitron 950 Triboindenter (Bruker Corporation, Massachusetts) and a Berkovich diamond probe at a constant loading rate of 1000 μN s^{-1} to obtain reduced modulus and hardness, where reduced modulus was converted to elastic modulus.[25] For NMs, continuous stiffness measurement (CSM) nanoindentation was performed using a Berkovich probe at a constant strain rate of 0.05 s^{-1} to measure hardness H and elastic modulus E via an iNano nanoindenter (KLA, California).[67] The 6×6 indent array with a maximum load of 50 mN was applied to each sample. Machine compliance and the tip area function were calibrated on a fused quartz reference sample before and after each test, following the procedure outlined by Oliver and Pharr.[67] Nix's model and Korsunsky's model were used to correct the influence of the substrate on the elastic modulus and hardness, respectively, using an averaged Poisson's ratio of 0.27 for the NM samples.[68–70] The properties of the substrate have been independently measured via the CSM technique, which was used for the deconvolution of the measured data. For both nanoindentation configurations, the elastic modulus and Poisson's ratio of the indenter are 0.07 and 1140 GPa, respectively.

Micropillar Splitting: Arrays of at least fifteen micropillars (nominal top diameter of ≈1 μm) were prepared for each sample by focused ion beam (FIB) milling with the Helios 5CX Dual Beam Microscope, using a previously developed preparation procedure that can minimize FIB-induced damage on the edge of pillars: five coarse milling steps have been employed using an ion current of 0.28 nA followed by a final refinement and shaping process involving a current of 7.7 pA.[36] The distance between each pillar is set to 10 μm. The aspect ratio (height-to-diameter) of the pillars was ensured to be greater than one, guaranteeing complete relaxation of the residual stress, if present, within the probing volume.

Sharp indentation using a diamond tip with a cube-corner geometry on the center of each pillar was performed at a constant loading rate of ≈0.033 mN s^{-1} until unstable propagation of a crack is achieved, thereby attaining the critical splitting load P_c, which appears as a burst in the load-displacement curve. The accurate positioning of the indenter at each pillar center was achieved in situ using a KLA nanoFLIP system equipped inside a FEI Helios NanoLab 600 Microscope. E-beam was used during positioning and switched off during testing to avoid possible beam damage.[71] From the attained crack propagation and failure, fracture toughness was computed through Equation (1).

$$K_c = \gamma \cdot \frac{P_c}{R^{\frac{3}{2}}} \tag{1}$$

Since γ coefficients were calculated assuming average film E/H ratios, the use of Equation (1) results in the estimation of "apparent" fracture toughness for the multilayer systems. Based on postmortem fracture morphology, only those pillars that were well centered (within the 10% threshold of the pillar-measured radius as described by Lauener et al.) and split into three parts were selected to calculate the apparent fracture toughness of the coatings.[36]

Vickers Indentation and Deformed Cross-Section Preparation: A minimum of five Vickers indents per sample were carried out using a LM-100 Microindentation Hardness Tester (Leco, Michigan) at a 0.245 N (25-gf) load. Samples for cross-sectional STEM were prepared using Helios G4 UXe PFIB Dual Beam system, following the procedure outlined in the "*Optical Design and as-Sputtered Characterization" Section*. A Cressington 108 Manual Sputter Coater (Ted Pella, Inc., California) was used for Pt-Pd protective coating. The lamellae were extracted using the Helios 5 Ga FIB UX DualBeam FIB, and TEM imaging was carried out using the Talos F200C G2 STEM.

Supporting Information

Supporting Information is available from the Wiley Online Library or from the author.

Acknowledgements

D.E.W. and A.M.H. would like to thank the Office of Naval Research (award no. N00014-18-1-2263 and N00014-23-1-2390). K.J. and Y.-T.S. acknowledge the Charles Lee Powell Foundation and the Core Center of Excellence in Nano Imaging (CNI) at USC for the characterization facilities. W.C. and E.R. gratefully acknowledge financial support in part by (a) the European Project "Integrated Computational-Experimental material Engineering of Thermal Spray coatings" (CoBRAIN) under the grant agreement no. 101092211, and (b) the PNRR Project "Infrastructure for Energy Transition and Circular Economy @ EuroNanoLab" (IENTRANCE) under the grant agreement no. IR0000027.

Conflict of Interest

The authors declare no conflict of interest.

Data Availability Statement

The data that support the findings of this study are available from the corresponding author upon reasonable request.

Keywords

Al_2O_3, fracture toughness, magnetron sputtering, nanolaminates, optical coatings

Received: May 11, 2025
Revised: August 28, 2025
Published online:

[1] C.-H. Liang, Y.-J. Chen, *Ceram. Int.* **2021**, *47*, 5177.
[2] D. C. Harris, *Optical Properties of Infrared Windows, Materials for Infrared Windows and Domes: Properties and Performance*, SPIE, Bellingham, Washington **1999**, ISBN: 9780819481016.
[3] H. K. Raut, V. A. Ganesh, A. S. Nair, S. Ramakrishna, *Energy Environ. Sci.* **2011**, *4*, 3779.
[4] K. Ye, Z. Li, *Corrosion* **2020**, *76*, 895.
[5] S. PalDey, S. C. Deevi, *Mater. Sci. Eng. A* **2003**, *342*, 58.
[6] J. M. González-Carmona, J. D. Triviño, Á. Gómez-Ovalle, C. Ortega, J. M. Alvarado-Orozco, H. Sánchez-Sthepa, A. Avila, *Ceram. Int.* **2020**, *46*, 24592.
[7] D. He, W. Li, L. Wang, Z. Lu, G. Zhang, Z. Cai, *Mater. Res. Express* **2019**, *6*, 116443.
[8] M. S. Konchady, A. Yarmolenko, D. M. Pai, J. Sankar, A. Kvit, *Int. J. Surf. Sci. Eng.* **2008**, *2*, 439.
[9] Z. R. Liu, Y. X. Xu, B. Peng, W. Wei, L. Chen, Q. Wang, *J. Alloys Compd.* **2019**, *808*, 151630.
[10] A. Thobor, C. Rousselot, C. Clement, J. Takadoum, N. Martin, R. Sanjines, F. Levy, *Surf. Coat. Technol.* **2000**, *124*, 210.
[11] M. Kong, J. Dai, J. Lao, G. Li, *Appl. Surf. Sci.* **2007**, *253*, 4734.
[12] G. Li, Y. Li, G. Li, *Thin Solid Films* **2012**, *520*, 2032.
[13] Y. Pan, L. Dong, N. Liu, J. Yu, C. Li, D. Li, *Appl. Surf. Sci.* **2016**, *390*, 406.
[14] D. E. White, C. D. Appleget, E. Rossi, M. Sebastiani, A. M. Hodge, *Mater. Des.* **2023**, *231*, 112014.
[15] I. Pana, C. Vitelaru, A. Kiss, N. C. Zoita, M. Dinu, M. Braic, *Mater. Des.* **2017**, *130*, 275.
[16] M. Mazur, D. Wojcieszak, J. Domaradzki, D. Kaczmarek, S. Song, F. Placido, *Opto-Electron. Rev.* **2013**, *21*, 233.
[17] X. Wang, T. Luo, Q. Li, X. Cheng, K. Li, *Solar Energy Mater. Solar Cells* **2019**, *191*, 372.
[18] B. Putz, S. Wurster, T. E. J. Edwards, B. Volker, G. Milassin, D. M. Tobbens, C. O. A. Semprimoschnig, M. Cordill, *Acta Astronautica* **2020**, *175*, 277.
[19] D. Garoli, L. V. Rodriguez De Marcos, J. I. Larruquert, A. J. Corso, R. P. Zaccaria, M. G. Pelizzo, *Appl. Sci.* **2020**, *10*, 7538.
[20] C. D. Appleget, A. M. Hodge, *Adv. Eng. Mater.* **2019**, *21*, 1801268.
[21] C. D. Appleget, A. M. Hodge, *Scr.* **2020**, *187*, 157.
[22] J. D. Lord, B. Roebuck, R. Morrell, T. Lube, *Mater. Sci. Technol.* **2010**, *26*, 127.
[23] B. Bhushan, X. Li, *Int. Mater. Rev.* **2003**, *48*, 125.
[24] A. S. M. Ang, C. C. Berndt, *Int. Mater. Rev.* **2014**, *59*, 179.
[25] A. C. Fischer-Cripps, *Nanoindentation*, 3rd ed., Springer New York **2011**, ISBN: 978-1-4419-9871-2.
[26] G. K. Beshish, C. W. Florey, F. J. Worzala, W. J. Lenling, *J. Therm. Spray Technol.* **1993**, *2*, 35.
[27] M. Kong, X. Wu, B. Huang, G. Li, *J. Alloys Compd.* **2009**, *485*, 435.
[28] C. D. Appleget, A. M. Hodge, *Opt. Mater. Express* **2020**, *10*, 850.
[29] A. F. Dericioglu, Y. F. Liu, Y. Kagawa, *J. Mater. Res.* **2009**, *24*, 3387.
[30] D. E. White, K. Jagadish, Y.-T. Shao, A. M. Hodge, *Thin Solid Films* **2025**, *815*, 140638.
[31] Z. Xu, Y. J. Zheng, F. Jiang, Y. X. Leng, H. Sun, N. Huang, *Appl. Surf. Sci.* **2013**, *264*, 207.
[32] J. Ast, M. Ghidelli, K. Durst, M. Göken, M. Sebastiani, A. M. Korsunsky, *Mater. Des.* **2019**, *173*, 107762.
[33] M. Sebastiani, K. E. Johanns, E. G. Herbert, G. M. Pharr, *Curr. Opin. Solid Mater. Sci.* **2015**, *19*, 324.
[34] M. R. Schoof, S. Karimi Aghda, C. F. Kusche, M. Hans, J. M. Schneider, S. Korte-Kerzel, J. L. Gibson, *J. Mater. Res.* **2023**, *38*, 3950.
[35] M. Sebastiani, K. E. Johanns, E. G. Herbert, F. Carassiti, G. M. Pharr, *Philos. Mag.* **2015**, *95*, 1928.
[36] C. M. Lauener, L. Petho, M. Chen, Y. Xiao, J. Michler, J. M. Wheeler, *Mater. Des.* **2018**, *142*, 340.
[37] P. F. Cesar, A. Della Bona, S. S. Scherrer, M. Tholey, R. van Noort, A. Vichi, R. Kelly, U. Lohbauer, *Dental Mater.* **2017**, *33*, 575.
[38] R. Bermejo, Y. Torres, A. Sanchez-Herencia, C. Baudín, M. Anglada, L. Llanes, *Acta Mater.* **2006**, *54*, 4745.
[39] M. Ghidelli, M. Sebastiani, K. E. Johanns, G. M. Pharr, *J. Am. Ceram. Soc.* **2017**, *100*, 5731.
[40] W. F. Hosford, *Mechanical Behavior of Materials*, Cambridge University Press, Cambridge **2005**, ISBN: 9780521846707.
[41] S. Kalácska, L. Pethö, G. Kermouche, J. Michler, P. D. Ispánovity, *Surf. Coat. Technol.* **2025**, *498*, 131817.
[42] B. Putz, T. E. J. Edwards, E. Huszar, P. A. Gruber, K. P. Gradwohl, P. Kreiml, D. M. Többens, J. Michler, *Adv. Eng. Mater.* **2023**, *25*, 2200951.
[43] J. H. Lu, B. Y. Chen, H. C. Tzou, in *2011 6th IEEE Int. Conf. on Nano/Micro Engineered and Molecular Systems*, IEEE, Kaohsiung, Taiwan **2011**, p. 45.
[44] J.-H. Lu, T.-W. Huang, C.-Y. Cheng, J.-W. Lee, C.-W. Chang, *J. Vacuum Sci. Technol. A* **2016**, *34*, 051513.
[45] C.-h. Park, Y. H. Kim, H. Jeong, B.-R. Won, H. Jeon, J.-h. Myung, *Ceram. Int.* **2023**, *49*, 32953.
[46] Q.-L. Xiao, C. Xu, S.-Y. Shao, J.-D. Shao, Z.-X. Fan, *Vacuum* **2008**, *83*, 366.
[47] A. F. Dericioglu, *Mater. Trans.* **2008**, *49*, 2714.
[48] P. Dubey, A. K. Battu, V. Shutthanandan, C. V. Ramana, *J. Minerals Met. Mater. Soc.* **2019**, *71*, 3711.
[49] E. Nichelatti, M. Montecchi, R. M. Montereali, *J. Non-Cryst. Solids* **2009**, *355*, 1115.
[50] A. Jiménez-Solano, M. Anaya, M. E. Calvo, M. Alcon-Camas, C. Alcaniz, E. Guillen, N. Martinez, M. Gallas, T. Preussner, R. Escobar-Galindo, H. Miguez, *Adv. Opt. Mater.* **2017**, *5*, 1600833.
[51] Y. Matsuoka, S. Mathonnèire, S. Peters, W. T. Masselink, *Appl. Opt.* **2018**, *57*, 1645.
[52] S. Chhajed, D. J. Poxson, X. Yan, J. Cho, E. F. Schubert, R. E. Welser, A. K. Sood, J. K. Kim, *Appl. Phys. Express* **2011**, *4*, 052503.
[53] O. Stenzel, O. Miloslav, *Optical Characterization of Thin Solid Films*, 1st ed., Springer Cham **2018**, ISBN: 9783319753249.
[54] F. Praud, T. Schmitt, O. Zabeida, S. Maïza, L. Martinu, M. Lévesque, *Thin Solid Films* **2021**, *736*, 138920.
[55] G. Abadias, E. Chason, J. Keckes, M. Sebastiani, G. B. Thompson, E. Barthel, G. L. Doll, C. E. Murray, C. H. Stoessel, L. Martinu, *J. Vacuum Sci. Technol. A* **2018**, *36*, 020801.
[56] Y. X. Wang, S. Zhang, *Surf. Coat. Technol.* **2014**, *258*, 1.
[57] W. D. Callister, *Materials science and engineering: An introduction*, 9th ed., John Wiley & Sons, New York **2014**, ISBN: 0471736961.
[58] M. Huff, *Micromachines* **2022**, *13*, 2084.
[59] M. Ghosh, A. Paul, R. Mandal, *Comprehensive Materials Processing*, 2nd ed., (Ed. S. Hashmi), Elsevier, Oxford **2024**, ISBN: 978-0-323-96021-2.
[60] C.-C. Lee, C.-L. Tien, W.-S. Sheu, C.-C. Jaing, *Rev. Sci. Instrum.* **2001**, *72*, 2128.
[61] E. Çetinörgü, B. Baloukas, O. Zabeida, J. E. Klemberg-Sapieha, L. Martinu, *Appl. Opt.* **2009**, *48*, 4536.

[62] F. Richter, H. Kupfer, P. Schlott, T. Gessner, C. Kaufmann, *Thin Solid Films* **2001**, *389*, 278.
[63] Q. Gao, S. Zhu, *Textbook of Medical Statistics: For Medical Students*, Springer Nature Singapore **2024**, ISBN: 9789819973903.
[64] Y. Cui, P. Huang, F. Wang, T. J. Lu, K. W. Xu, *Thin Solid Films* **2015**, *584*, 270.
[65] T. E. J. Edwards, T. Xie, N. Maria della Ventur, D. Casari, C. Guerra, E. Huszar, X. Maeder, J. J. Schwiedrzik, I. Utke, L. Petho, J. Michler, *Acta Mater.* **2022**, *240*, 118345.
[66] P. Hollmann, G. Grumbt, R. Zenker, H. Biermann, K. Weigel, K. Bewilogua, G. Bräuer, *Surf. Coat. Technol.* **2018**, *338*, 75.
[67] W. C. Oliver, G. M. Pharr, *J. Mater. Res.* **1992**, *7*, 1564.
[68] M. F. Doerner, W. D. Nix, *J. Mater. Res.* **1986**, *1*, 601.
[69] A. M. Korsunsky, M. R. McGurk, S. J. Bull, T. F. Page, *Surf. Coat. Technol.* **1998**, *99*, 171.
[70] Z. Wei, G. Zhang, H. Chen, J. Luo, R. Liu, S. Guo, *J. Mater. Res.* **2009**, *24*, 801.
[71] S. Bruns, L. Petho, C. Minnert, J. Michler, K. Durst, *Mater. Des.* **2020**, *186*, 108311.
[72] The Resource. 2000–2022, https://azom.com.
[73] P. Baral, S. Jaddi, H. Wang, A. Orekhov, N. Gauquelin, A. Bagherpour, F. Van Loock, M. Coulombier, A. Favache, M. Rusinowicz, J. Verbeeck, S. Lucas, J.-P. Raskin, H. Idrissi, T. Pardoen, *Nat. Commun.* **2025**, *16*, 1355.
[74] R. N. Chan, B. R. Stoner, J. Y. Thompson, R. O. Scattergood, J. R. Piascik, *Dental Mater.* **2013**, *29*, 881.
[75] D. W. Stollberg, J. M. Hampikian, L. Riester, W. B. Carter, *Mater. Sci. Eng. A* **2003**, *359*, 112.